Available online at www.sciencedirect.com

SCIENCE DIRECT®

Earth and Planetary Science Letters 225 (2004) 131–146

EPSL

www.elsevier.com/locate/epsl

Receiver function tomography of the central Tien Shan

Lev P. Vinnik[a,1], Christoph Reigber[b,2], Igor M. Aleshin[a,3], Grigoriy L. Kosarev[a,3], Mikhail K. Kaban[b,*], Sergey I. Oreshin[a,3], Steven W. Roecker[c,4]

[a] *Institute of Physics of the Earth, B. Grouzinskaya, 10, 123995, Moscow, Russia*
[b] *GeoForschungsZentrum Potsdam (GFZ), Dept. 1, Telegrafenberg, A 17, Potsdam D-14473, Germany*
[c] *Rensselaer Politechnic Institute, Dep. Earth and Environmental Sciences, 110 8th St., JSC 1W06, Troy, NY 12180-3522 USA*

Received 9 January 2004; received in revised form 13 May 2004; accepted 28 May 2004
Available online 24 July 2004
Editor: V. Courtillot

Abstract

To obtain an image of the deep structure of the Tien Shan in central Asia, we invert P and S receiver functions jointly for almost 40 local broad-band seismograph stations. The inversion is performed using a simulated annealing technique. The combined inversion is an improvement on earlier studies, where P and S receiver functions were inverted separately. Using this approach, we deal with structural imaging problems that are usually investigated with teleseismic body wave and surface wave tomography techniques. We demonstrate that the uppermost mantle in the north of the central Tien Shan is composed of a high-velocity lid a few tens of kilometers thick above a pronounced low-velocity zone. The crustal structure in this region provides evidence of magmatic underplating. These features are likely related to a small plume that is manifested by basaltic eruptions of Cretaceous–Paleogene age. The low-velocity layer is also found in a southeast trending corridor, which may correspond to the Bachu uplift in the Tarim basin. Crustal thickness beneath the orogen varies from about 45 to about 70 km. The smallest values, most likely inherited from the pre-orogenic era, are found in a neighborhood of the Talas–Fergana fault. Similar values are characteristic of the Kazakh shield in the north and the Tarim basin in the south. The largest values are found beneath the bounding ranges. We infer that uplift of the central Tien Shan is unlikely to be caused by crustal shortening alone.

Keywords: receiver functions; Tien Shan; lithosphere; Moho

1. Introduction

The Tien Shan is the world's largest and most active intracontinental orogen (Fig. 1). The ancestral Tien Shan was formed by convergence of a few continental blocks during the late Palaeozoic [1]. In the Mesozoic the mountains were peneplenized [2–6]. Tectonic activity resumed at about 20 Ma [7], and at present, the central Tien Shan is shortening at a rate of

* Corresponding author. Tel.: +49-331-288-1172; fax: +49-331-288-1111.
E-mail addresses: vinnik@dubna-2.scgis.ru (L.P. Vinnik), reigber@gfz-potsdam.de (C. Reigber), ima@ifz.ru (I.M. Aleshin), kosarev@dubna-2.scgis.ru (G.L. Kosarev), kaban@gfz-potsdam.de (M.K. Kaban), oreshin@dubna-2.scgis.ru (S.I. Oreshin), roecks@rpi.edu (S.W. Roecker).
[1] Tel.: +7-95-2549325; fax: +7-95-2556040.
[2] Tel.: +49-331-288-1100; fax: +49-331-288-1111.
[3] Tel.: +7-95-2549405; fax: +7-95-2556040.
[4] Tel.: +1-518-2766773; fax: +1-518-2762012.

0012-821X/$ - see front matter © 2004 Elsevier B.V. All rights reserved.
doi:10.1016/j.epsl.2004.05.039

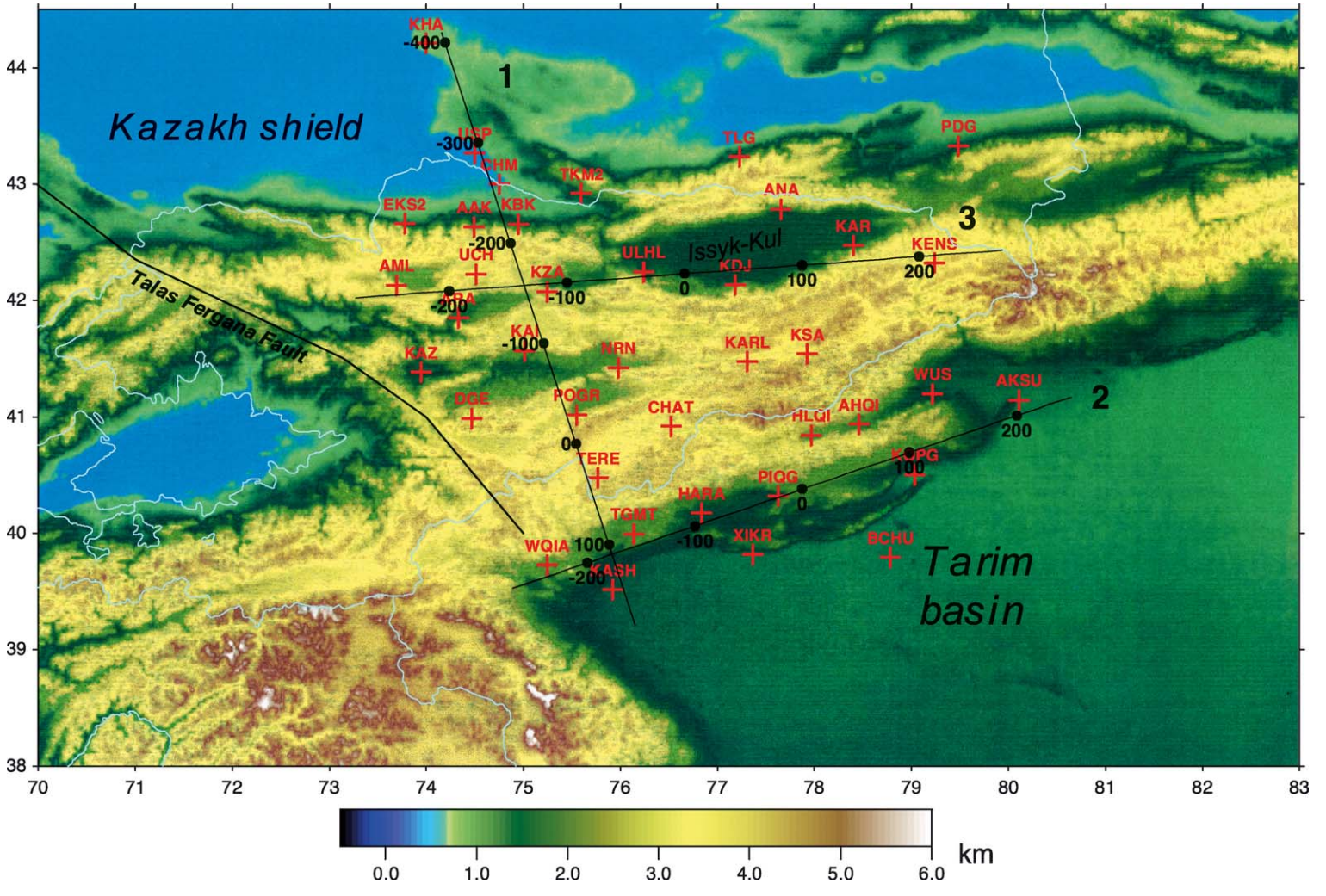

Fig. 1. Map of the region with seismograph stations (red crosses). Straight lines are the profiles, along which cross-sections of the velocity model are shown in Figs. 15–17.

about 20 mm/year [8,9]. The revival of tectonic activity is usually attributed to the India–Eurasia collision [10], although the details about how these are related are controversial.

Near-surface deformations are documented by geologic studies [11–13], but the related structures in the deep crust and the upper mantle are still not well resolved. According to previous seismic studies, the Moho depth varies in a range of about 25 km [14–16]. Body wave travel time tomography with local seismic sources reveals a pronounced lateral heterogeneity of crustal structure [17,18]. P receiver functions reveal among other features a laterally variable fractured surficial layer [19]. The transition from the mantle to the crust is either sharp (to the West of the Talas–Fergana fault) or gradual (in the central Tien Shan to the East of the fault [20]). Seismic inhomogeneities in the crust correlate with variations of electric conductivity [21]. As indicated by teleseismic P travel time residuals, seismic velocities in the upper mantle to the East of the Talas–Fergana fault are low relative to those in the West [22]. S receiver functions reveal a high-velocity mantle lid and an underlying low-velocity layer at a number of locations [16]. There is evidence of seismic azimuthal anisotropy in the upper mantle. The anisotropy varies laterally [23,24] and with depth [25].

The potential for detailed seismic studies was greatly enhanced by operation of a number of broad-band digital seismograph stations (Fig. 1). The digital data were processed for crustal and upper mantle structures with the P and S receiver techniques [15,16,19,20,26]. The P receiver function technique is relatively well known [27,28], and used in seismic studies worldwide. This technique relies mainly on Ps seismic phases that are converted from P to S at seismic discontinuities in a vicinity of the seismograph station (Fig. 2). The most reliable features in the related velocity profiles are discontinuities and zones of high gradient. Interference between the Ps phases from deep discontinuities and multiple reflected or scattered phases from shallow discontinuities is the main shortcoming of this technique. As a result, strong multiples from the Moho and other crustal boundaries can be easily mistaken for the Ps phases from discontinuities in the uppermost mantle. Similarly, if the uppermost crust is composed of loose sediments, the Ps phase from the Moho can be hidden in the multiples from the base of the sediments.

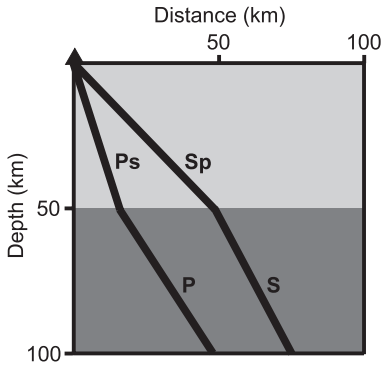

Fig. 2. Ray diagram for Ps and Sp phases. The scales for the distance and depth are similar. Vp and Vs are 6.6 and 3.8 km/s for the upper layer (crust) and 8.0 and 4.5 km/s for the mantle. Epicentral distances are 50° and 70° for the P and S waves, respectively.

The S receiver function technique that exploits S-to-P (Sp) converted phases was introduced recently [29] and has been used in a few studies [16,30,31]. A significant advantage of S receiver functions over the P receiver functions is that the multiples from shallow discontinuities arrive later than the Sp phases from deep discontinuities. On the other hand, shorter-period P receiver functions may resolve structures in the upper crust better than the S receiver functions. Moreover, the Ps and Sp phases at the same epicentral distance have different apparent velocities, and they can sample the same block of the earth medium at different angles of incidence. P and S receiver functions are therefore complementary, suggesting that a simultaneous inversion would result in a better constrained model. In this paper, we describe the results of such a joint inversion using data from practically all of the seismograph stations in the central Tien Shan.

2. Method

Methodologies for obtaining receiver functions are described in detail elsewhere; here, we give only a brief review. To calculate P receiver functions, the

individual 3-component seismograms are decomposed into the L (or P) and Q (or SV) components. The L axis is parallel to the principal direction of the P wave particle motion in the wave propagation plane. The Q axis is perpendicular to P in the same plane and is optimal for detecting Ps phases. Both components are deconvolved by the L component, and the deconvolved components are stacked to reduce noise. Calculations of the S receiver functions involve decomposition of the seismograms into the components that are termed Q (or SV) and L (or P), though they are defined differently from those in the P receiver functions. The Q axis corresponds to the principal S particle motion direction in the wave propagation plane. The L axis is perpendicular to Q in the same plane and is optimal for detecting the Sp converted phases. Both components are deconvolved by the Q component, and the deconvolved components are stacked to reduce noise. The angles i_P between the principal direction of the P wave motion and the vertical direction (for the P receiver functions) and i_{SV} between the principal direction of S wave motion in the wave propagation plane and the radial direction (in the S receiver functions) are determined by analyses of the related covariance matrices.

As in similar studies, we assume that the earth's medium in a vicinity of the seismograph station is laterally homogeneous and isotropic; heterogeneity is characterized by joining locally homogeneous blocks. For the same discontinuity, the Sp ray piercing point is at a larger distance from the seismograph station (Fig. 2), but we assume that the P and S receiver functions sample the same homogeneous block of the Earth's medium. A trial model for the block is described by P and S velocities Vp and Vs, density ρ and a thickness of each plane layer. To model the receiver functions, we calculate for a trial model the synthetic Q and L components for the P and S receiver functions, respectively:

$$Q_{P,syn}(t,\boldsymbol{m},c_p) = \frac{1}{2\pi}\int_{-\infty}^{\infty}\frac{H_{P,Q}(\omega,\boldsymbol{m},c_p)}{H_{P,L}(\omega,\boldsymbol{m},c_p)}L_{P,obs}(\omega)\exp(i\omega t)d\omega \quad (1)$$

$$L_{SV,syn}(t,\boldsymbol{m},c_{SV}) = \frac{1}{2\pi}\int_{-\infty}^{\infty}\frac{H_{SV,L}(\omega,\boldsymbol{m},c_{SV})}{H_{SV,Q}(\omega,\boldsymbol{m},c_{SV})}Q_{SV,obs}(\omega)\exp(i\omega t)d\omega \quad (2)$$

Here, t is time, ω is angular frequency, $\boldsymbol{m}$ is the vector of model parameters, angles i_P and i_{SV} are included in $\boldsymbol{m}$, c_P and c_{SV} are assumed apparent velocities, indices "obs" and "syn" correspond to the stack of the actual receiver functions and their synthetic analogues, respectively, and H are theoretical transfer functions for the stack of plane layers. The theoretical transfer functions are calculated with the aid of Thomson–Haskell matrix algorithm [32].

For each trial model, we calculate penalty function E:

$$E(\boldsymbol{m}) = (1-\alpha)\,\|\,Q_{P,obs}(t) - Q_{P,syn}(t,\boldsymbol{m},c_P)\,\| + \alpha\,\|\,L_{SV,obs}(t) - L_{SV,syn}(t,\boldsymbol{m},c_{SV})\,\| \quad (3)$$

where α defines relative weights of the P and S receiver functions. The optimum model provides minimum of E. In practice, the value of α is usually close to 0.5.

A search for the optimum model is conducted by Adaptive Simulated Annealing algorithm (ASA) [33]. The models generated from gradient-based methods of optimization that were often used for a similar purpose in the past [20] can depend on the starting model because the error surface may have several local minima. By contrast, the ASA algorithm makes a search for the global minimum. It belongs to the group of directed Monte Carlo methods that explore a wide space of possible solutions much more efficiently than do pure Monte Carlo random search techniques. This algorithm was previously applied to a number of geophysical problems, including the inversion of P receiver functions [34].

We conducted a number of tests to understand how best to adjust the parameters of the inversion algorithm. For example, the model can be composed of layers with either fixed or unknown thickness. We prefer the latter parameterization because it usually provides satisfactory results with a smaller number of

layers (Fig. 3). Our tests demonstrate that, generally, the Vp/Vs ratio cannot be determined uniquely from the receiver functions alone. There is a possibility of constraining the ratio between the average crustal velocities [35], but this relies on high-quality recordings of crustal multiples. In actual data such a quality is rare, particularly in active tectonic regions. To reduce the number of the unknowns, we fix the Vp/Vs ratio at reasonable estimates: 1.8 for the mantle and the uppermost low velocity crustal layer; 1.73 for the rest of the crust. These values are close to those in standard Earth model IASP91 [36]. Further tests (next Section) indicate that these values provide better results than do ratios independent of depth. Density cannot be inferred from the receiver functions and was assumed to follow the Birch equation.

Angles i_P and i_{SV} are known for each individual receiver function but not for the stacked ones. In the inversion, these angles are allowed to vary within a few degrees of their respective average values. The values of apparent velocity in individual recordings spread over a wide range. The optimum results of inversion of the stacked receiver functions were obtained by using the average value for the P receiver functions (usually around 17 km/s) and an intermediate value between those for S and SKS for the S receiver functions (13.2 km/s).

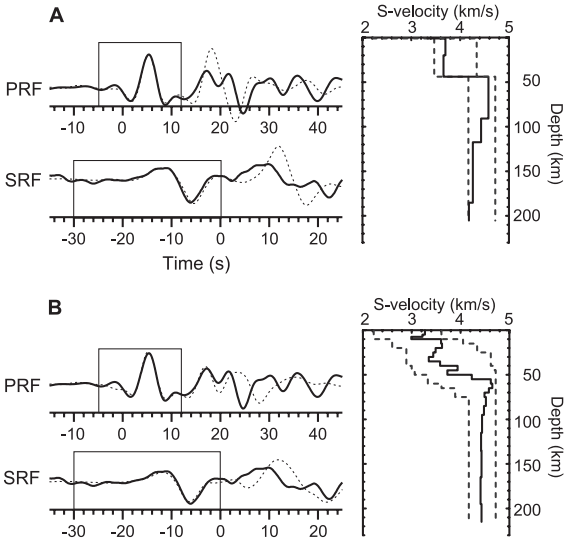

Fig. 3. Example of inversions of the P and S receiver functions for a model composed of several layers of variable thickness (A) and 34 thin layers with a fixed thickness (B). The actual receiver functions and their synthetic analogues are plotted on the left by solid and dash lines, respectively. Time windows for the inversion are shown by rectangles. The velocity profiles and the velocity bounds for inversion are shown on the right by solid and dash lines, respectively. The bounds for the layer thickness in A: 10–30 km for the two upper two layers, 10–50 km for the others.

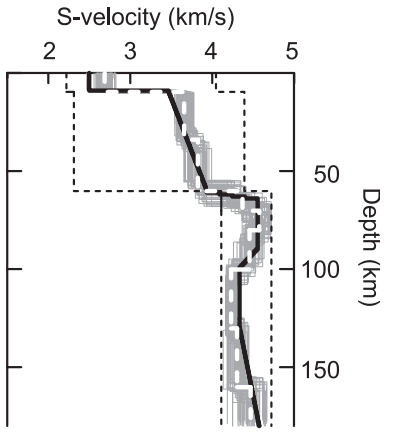

Fig. 4. Estimating the standard error of inversion by numerical experiment. Trial P and S receiver functions are obtained by summation of the theoretical receiver functions for the model shown by solid black line and of random Gaussian noise. The Q and L components of the P and S received functions, respectively, are normalized to the amplitudes of the L and Q components. The RMS value of the noise is 0.01. Individual solutions for 50 tests are shown by grey; the average is white. The bounds for velocity are shown by thin dash lines.

The accuracy of the method was tested by adding random noise to the synthetic receiver functions and comparing the resulting models with the input model (Fig. 4). The spectrum of the noise was taken similar to the spectrum of the L and Q components of the P and S receiver functions, respectively. Our estimates of the standard errors of the amplitude of normalized S and P receiver functions are on the order of 0.01, and we adopted this value for the RMS amplitude of the noise. The related standard errors of the S velocity models appear to be on the order of 0.1 km/s.

3. Data and results

The seismograph stations in the central Tien Shan (Fig. 1) belong to the networks KNET (9 stations),

GSN/IRIS (stations AAK and TLG), GEOSCOPE (station WUS) and GHENGIS (28 stations) [15]. The GHENGIS network operated for about 18 months and the others from several years to up to more than 10 years (station WUS). Teleseismic events used in this study are located in the back azimuth sector from 90° to 120°. This sector provides an exceptionally large number of recordings in a broad epicentral distance range. Most of the related receiver functions were calculated previously [16,19,25].

P receiver functions (Fig. 5) are obtained in a distance range from 40° to 100°. The usual number of the stacked functions is on the order of a few tens. Seismograms with dominant periods of around 1–2 s are severely contaminated by random wave scattering. This effect is less significant at longer periods, and by

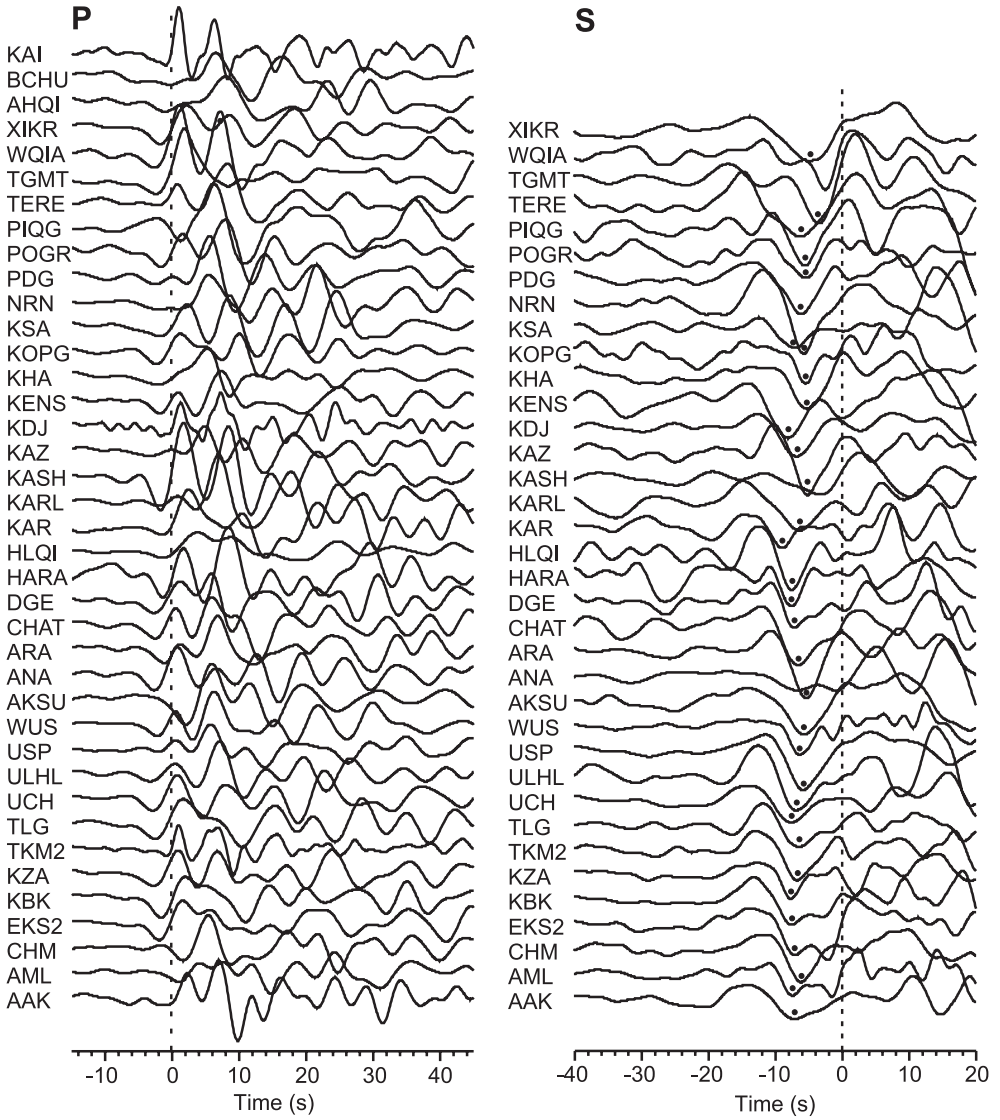

Fig. 5. Summary P (left) and S (right) receiver functions. The receiver functions of KNET and other long-term stations are at the bottom of the figure. For a few stations at the top, there are only P receiver functions. The supposed Sp phases from the Moho in the S receiver functions are marked by dots.

low-pass filtering, we suppress the periods shorter than 5 s. The Ps converted phase from the Moho is expressed as a phase with upward motion at a time of 6–8 s. At many stations, the upward motion is observed at a time of 1–3 s. This is the Ps converted phase from the bottom of a surficial fractured zone or, at some stations in China, from the bottom of a sedimentary layer [19].

S receiver functions (Fig. 5) were obtained at distances from 65° to more than 100°. At smaller distances, the SP phase (reflected from the earth's surface between the source and the receiver) arrives with a small delay relative to S. The dominant period in the S receiver functions (around 10 s) is longer than in the P receiver functions. The average number of the stacked S receiver functions varies between about 25 for the GHENGIS network to 70–90 for the other stations, and the signal/noise ratio in the stacked functions for the long-term stations (bottom of Fig. 5) is higher than for the others. For a few stations of the GHENGIS network, the amount of useful recording was not sufficient for S receiver functions to be determined. The Sp converted phase from the Moho boundary is expressed as a prominent downward motion with a lead time of several seconds. Another prominent phase is expressed as the upward motion at a time around −14 s. This motion is especially well seen in the data of the KNET stations and corresponds to the upper boundary of the mantle low velocity layer [16].

Combined processing of the P and S receiver functions is demonstrated by the following examples. A typical number of trial models in the inversion procedure are 10^4. Station USP (Fig. 6) is one of the 'easy' ones. Inversion of the P receiver function is shown for the time intervals ending at 12 and 30 s. The shorter interval includes the arrivals of the Ps phases from discontinuities not deeper than about 100 km. Multiple reflections present within this interval are related only to the upper crust, whereas those related to the Moho arrive much later. The longer interval includes Ps phases from discontinuities not deeper than about 250 km and multiple reflections from the Moho. Velocity in the crust could vary in a wide range, but not exceed 3.6 km/s in the uppermost zone a few kilometers wide. The highest and the lowest velocity in the upper mantle were fixed at 4.1 and 4.7 km/s. Layer thickness was bounded by 1–

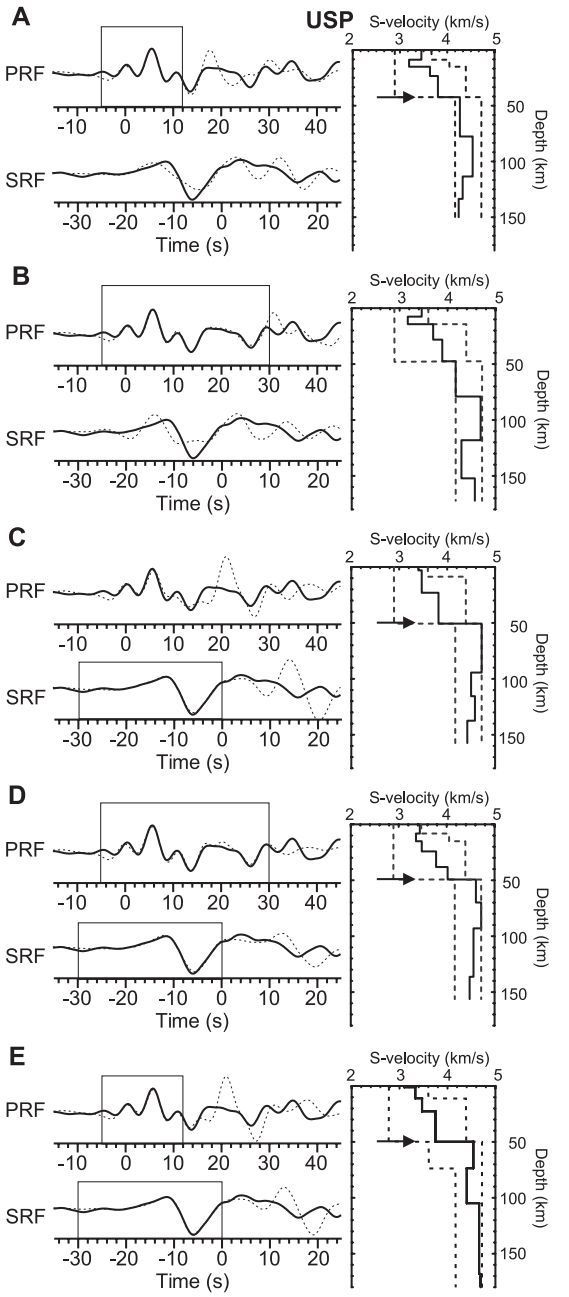

Fig. 6. Actual (solid lines) and theoretical (dash lines) receiver functions (left) and the corresponding S velocity models (right) of station USP. Time windows for the inversion are shown by rectangles. Boundary values for the velocity are shown by dash lines. Positions of the Moho in the models are shown by arrows. A, B—inversion of the P receiver functions; C—inversion of the S receiver function; D, E—combined inversion of the P and S receiver functions.

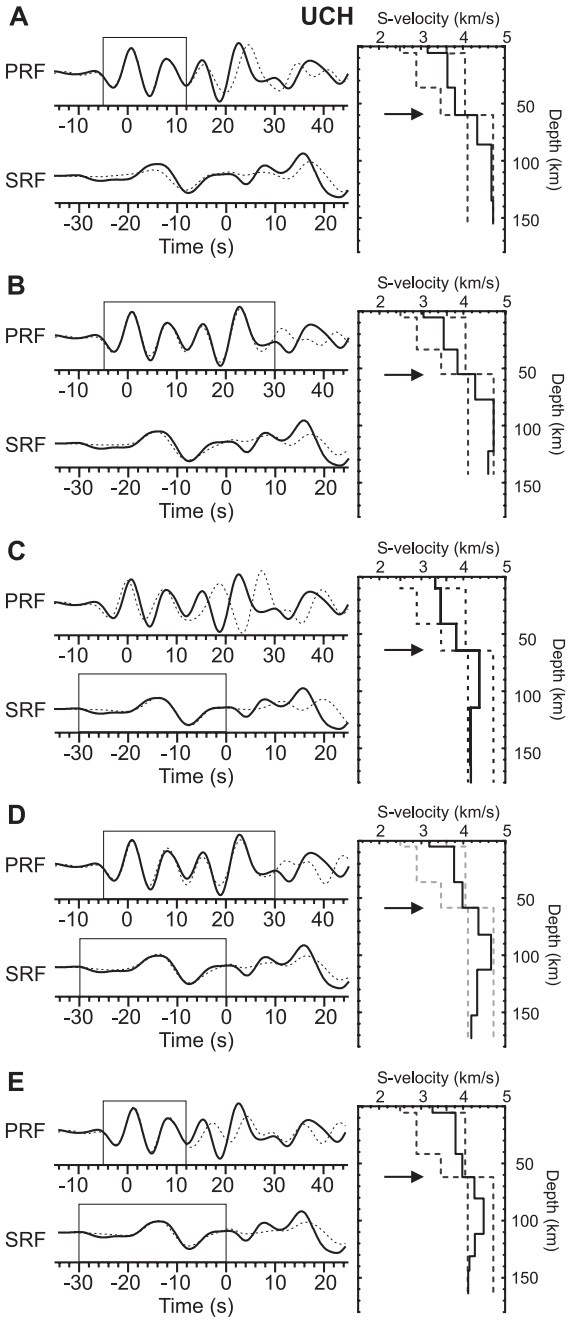

Fig. 7. The same as in Fig. 6, but for station UCH.

10 km in the two upper layers, 10–30 km in the other crustal layers, 20–50 km in the mantle. Comparable bounds were adopted for the other stations.

The optimum models for the P receiver functions in the two time intervals differ in details, and the Moho depth of 40 km (for the short time interval)

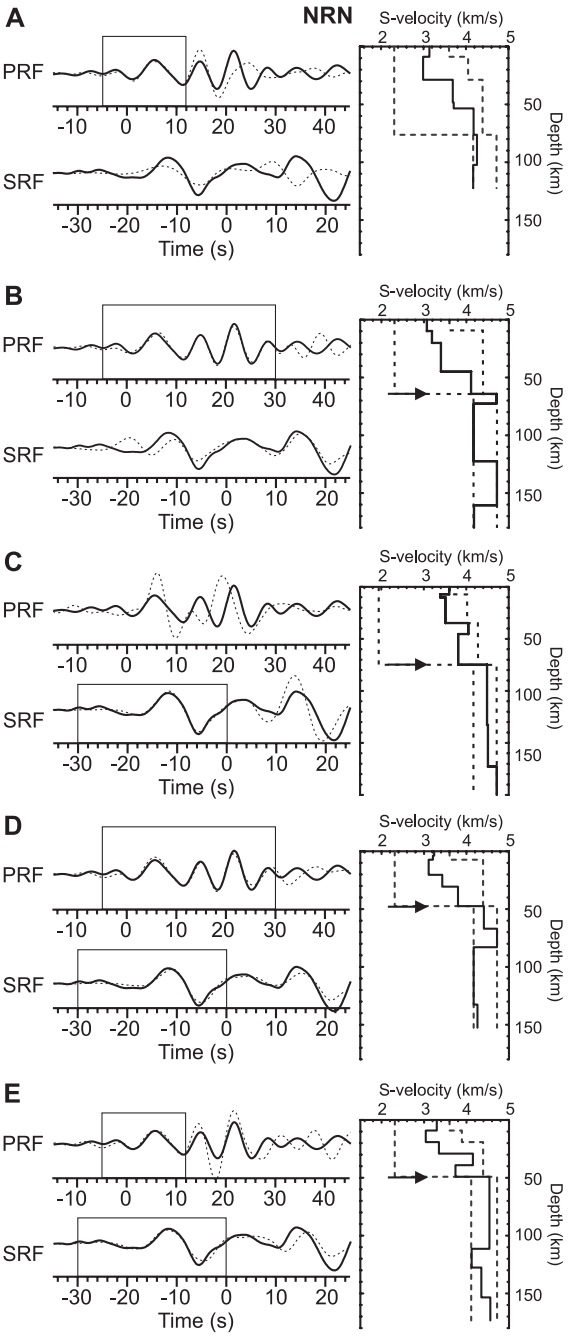

Fig. 8. The same as in Fig. 6, but for station NRN.

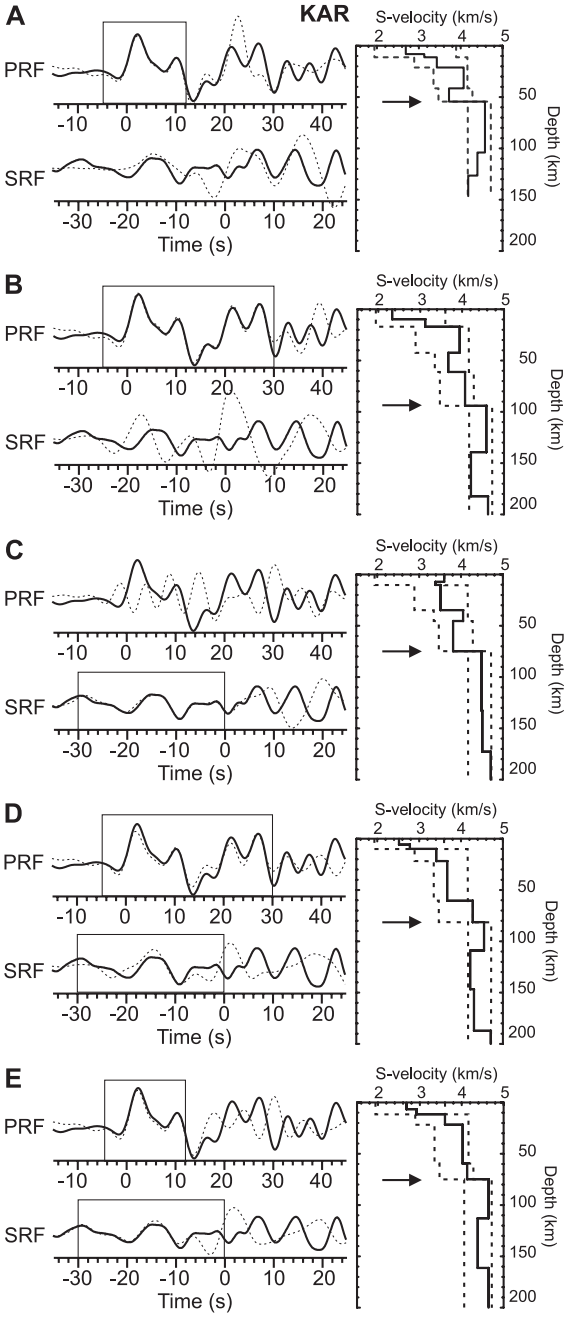

Fig. 9. The same as in Fig. 6, but for station KAR.

becomes uncertain for the longer interval. The theoretical S receiver functions for these models disagree with the observed function. However, the best model for the S receiver function makes a good prediction for the P receiver function in the short time interval. The models obtained by the combined inversion of the S and P receiver functions in the two intervals differ in details, but some of their properties (crustal thickness, average velocities in the upper and the lower crust and in the upper mantle) are close. In the model obtained by the combined inversion for the short interval the velocities are not restrained by the bounding values, except in two very narrow intervals.

A generally similar relation between the P and S receiver functions is observed at another 'easy' station UCH (Fig. 7). The optimal model for the P receiver function in the long time interval makes a surprisingly good prediction for the S receiver function, and the optimal model for the S receiver function makes a reasonable prediction for the P receiver function in the

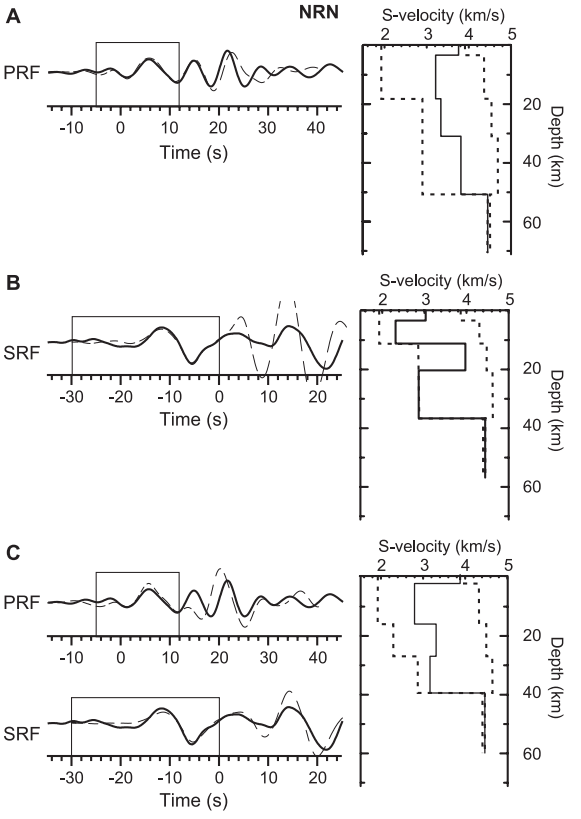

Fig. 10. Inversion of receiver functions of station NRN for the crustal model; the mantle is represented by half-space with fixed velocities: A—P receiver function; B—S receiver function; C—combined inversion of the P and S receiver functions.

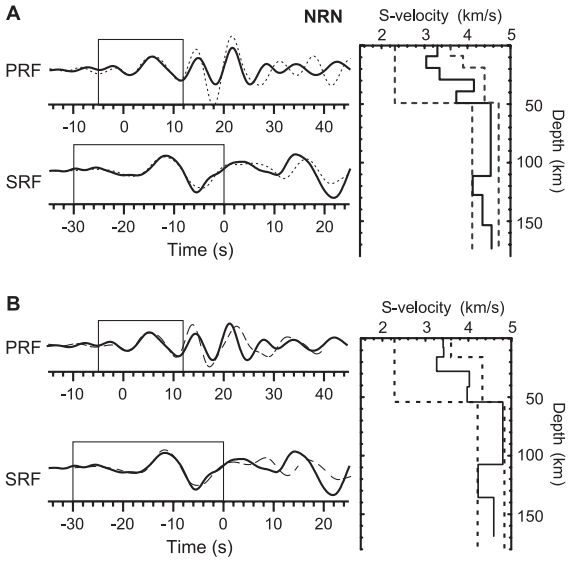

Fig. 11. Combined inversion of the receiver functions of station NRN for the depth dependent Vp/Vs ratio (A) and for the constant ratio of 1.75 (B).

short time interval. Two models obtained by the combined inversion of the P and S receiver function are fairly close, and both contain a pronounced low velocity layer in the upper mantle. The Moho boundary in both models is at a depth of around 60 km.

More complicated data are obtained at station NRN (Fig. 8). The models for the P receiver function predict theoretical S receiver functions that are very different from the actual one. Similarly, the model obtained from the S receiver function makes a very poor prediction for the P receiver function in both time intervals. Moreover, the models for the P receiver function in the two intervals differ in substantial details. However, both models obtained by the combined inversion have the same Moho depth and a pronounced low velocity layer in the upper mantle.

Another complicated set of data is obtained at station KAR (Fig. 9). The models for the P receiver function in the two time intervals differ in the Moho depth (55 versus 95 km) and in other significant details. The model for the short interval provides a

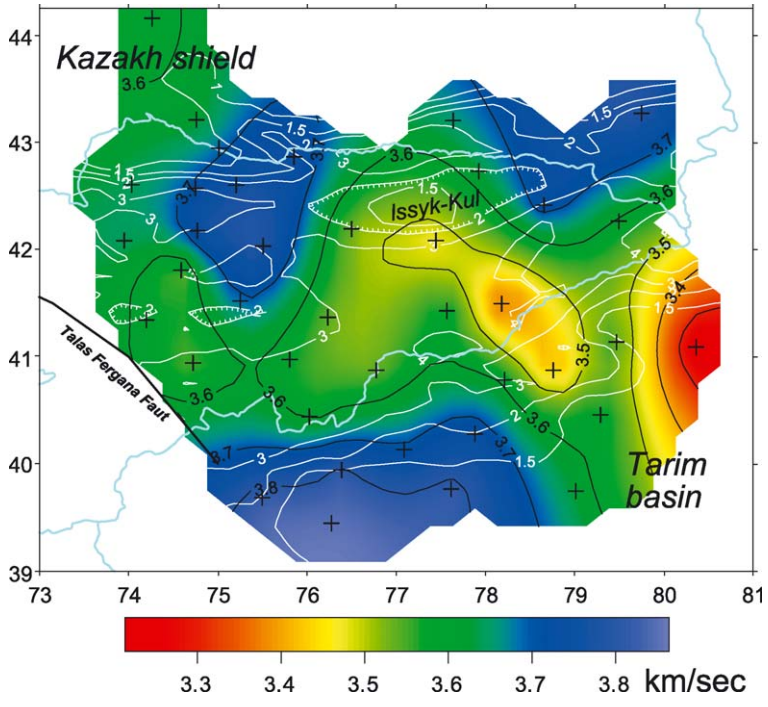

Fig. 12. Averaged S velocity within the crust in the depth interval from 10 km to 35 km. Smoothed topography is shown by white contours; the related numbers is altitude in kilometers. Locations of the stations are shown by black crosses.

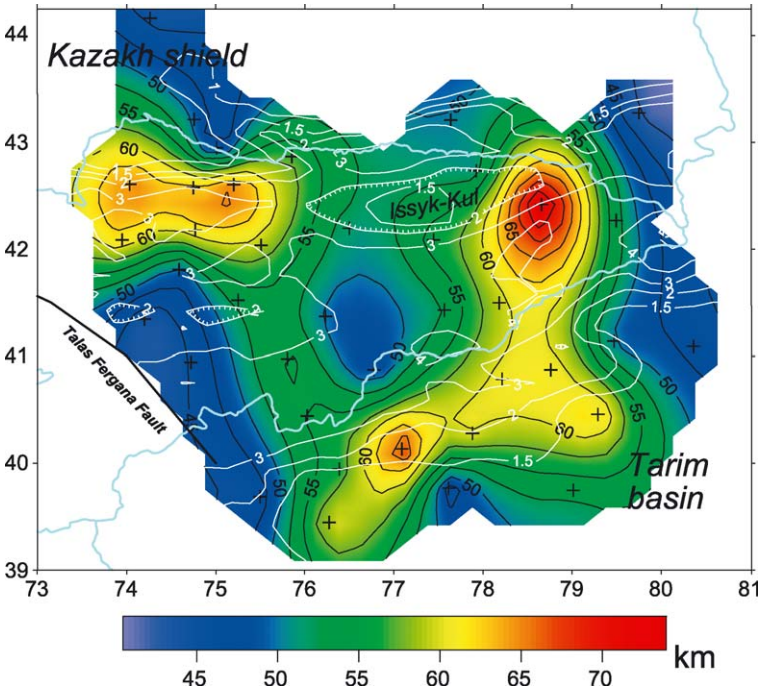

Fig. 13. Thickness of the crust. Smoothed topography and locations of seismograph stations are shown like in Fig. 12.

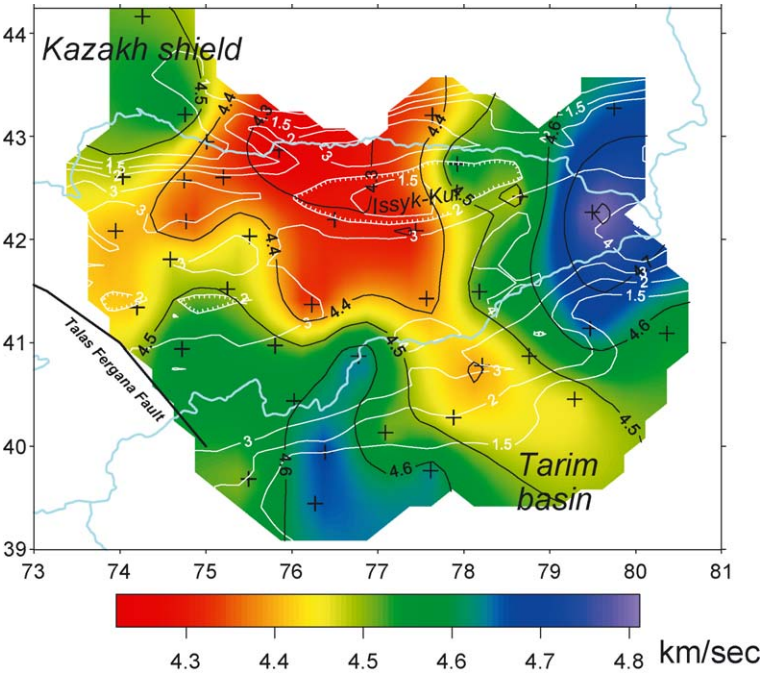

Fig. 14. The same as in Fig. 12, but for the mantle in the depth interval from 110 to 130 km.

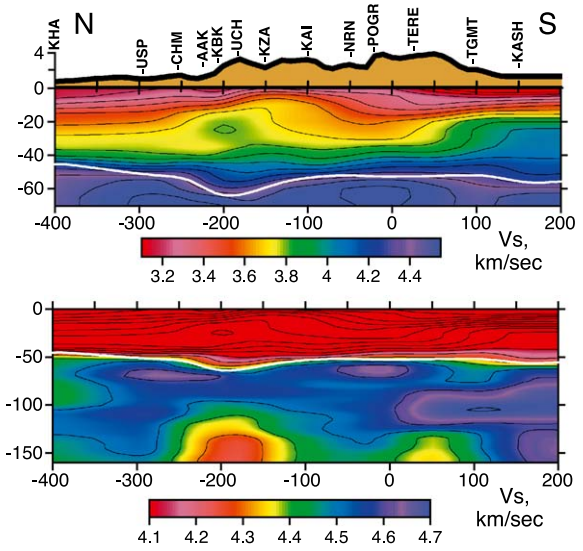

Fig. 15. Cross-sections of the S velocity model along the line 1 in Fig. 1 for the crust (top) and for the crust and mantle (bottom). Topography along the line is shown at the top. The stations are from the corridor ± 50 km wide.

much better prediction for the S receiver function, than the other one. The model for the S receiver function leads to a poor prediction for the P receiver function. The combined inversion failed for the long time interval, but an acceptable model was obtained for the short interval. Both models show very deep Moho (around 70 km) and a low-velocity layer in the upper mantle.

The long time interval in the P receiver functions of 'complicated' stations, like NRN and KAR, apparently contains waves randomly scattered by topographic relief and other scatterers in a large region. These phases cannot be accounted for by plane layer models. Therefore, we prefer the short time interval that is less contaminated by the effects of lateral heterogeneity. Then the models in the interval from the earth's surface to a depth of about 100 km are constrained by both P and S receiver functions, whereas at larger depths, they are constrained mostly by the S receiver functions.

The models for many stations contain a pronounced low velocity layer in the uppermost mantle. This feature is determined by the upward motion in the S receiver functions at a time around 14 s (Fig. 5). A question may arise, however, if both P and S receiver functions at such stations can be explained by crustal structures only. A typical test (Fig. 10) demonstrates that the P receiver function indeed can be explained by the crustal structure. However, the best model provides a poor approximation of the S receiver function. Moreover, S velocities in the crustal model obtained by the joint inversion (almost 4.0 km/s near the surface and 2.8 km/s underneath) would be difficult to explain with a realistic composition and temperature.

The question of the optimum Vp/Vs ratio was addressed in the preceding section. A test (Fig. 11) demonstrates a relation between the solutions that are obtained with the adopted values of the ratio and a ratio fixed at 1.75 independently of depth. In the last model, the Vs values in the uppermost mantle seem too high to be accepted.

For every station, we tested models with a varying number of layers and selected one with the minimum number of layers that was sufficient to reach the threshold of around 0.01 for the penalty function E. In several cases, the average S velocity in the intermediate crust (between 10 and 35 km) appeared to be far outside a realistic range of Vs = 3.6 ± 0.2 km/s (Vp = 6.2 ± 0.4 km/s). These models were forced to remain within a realistic range by changing the bounding velocity values in the inversion procedure.

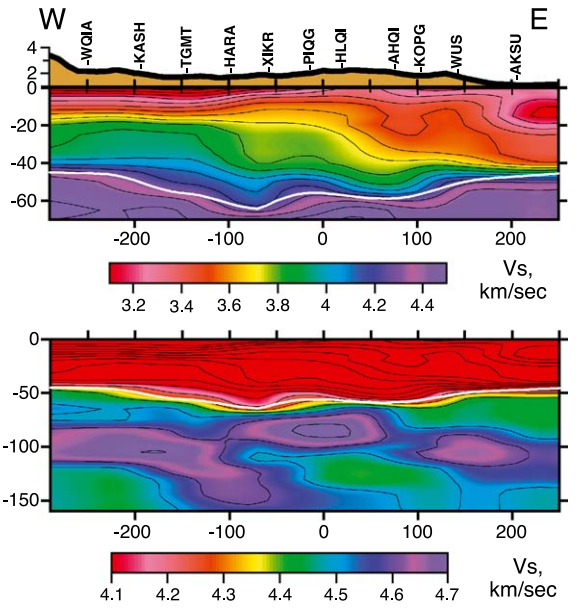

Fig. 16. The same as in Fig. 15, but for the line 2 in Fig. 1.

To visualize the results of the inversion, the results for every station were attributed to coordinates corresponding to the average of the Ps and Sp piercing points at the Moho. To obtain a 3-D velocity model from the individual 1-D velocity models, each individual model was smoothed with a Gaussian filter. Then for any fixed depth the individual models were interpolated with the standard Kriging technique for a linear isotropic variogram model [37]. The same technique was used to map the Moho depth. To construct the map of the Moho depth, we assumed for the lowest Vs at the top of the upper mantle (or the highest Vs at the bottom of the crust) the boundary value of 4.2 km/s. To some extent, this value is arbitrary, but it affects estimates of the Moho depth only at stations ARA, KOPG and PIQG, where the Moho corresponds to the Vs around 4.2 km/s. The estimates of the Moho depth at these stations are close to those at the neighboring stations, where it is defined robustly.

The average S velocity in the intermediate crust (Fig. 12) is usually in a realistic range; the only exception is in the southeastern corner of the region (station AKSU). The Moho depth (Fig. 13) varies between 40 and more than 70 km. Average back azimuth of our seismic events (105°) is not much different from the prevailing strike of the mountain ridges. In this direction, the crustal thickness usually varies at a rate of not more than a few kilometers per 50 km of distance, in agreement with the assumption of approximate lateral homogeneity in our method. The largest and the most reliably determined variations of Vs in the mantle (between 4.2 and 4.7 km/s) are found at depths of 110–130 km (Fig. 14). The main features of the preferred crust and mantle model are further illustrated by the vertical cross-sections to a depth of 160 km (Figs. 15–17). Interpolated velocity values in the cross-sections differ from the closest initial values by less than 0.05 km/s, and no substantial artifacts were noted in the intervals between the stations within the main area.

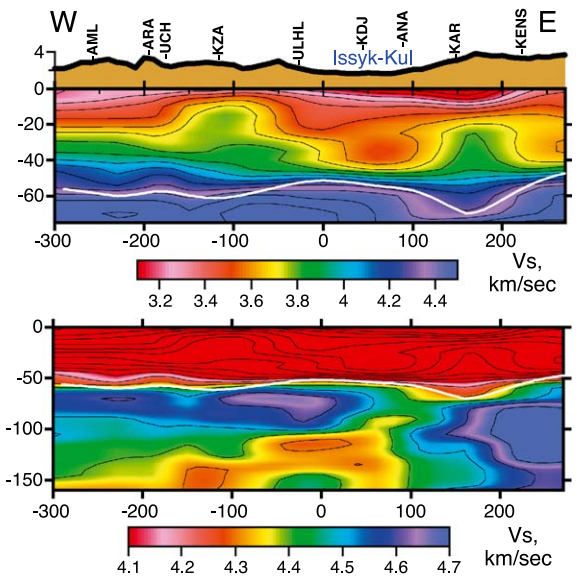

Fig. 17. The same as in Fig. 15, but for the line 3 in Fig. 1.

4. Discussion: tectonic implications of the seismic data

The methodology of our study still is in a state of development and leaves room for improvement. Nevertheless, the obtained results seem to be robust and deserve discussion. By combining P and S receiver functions from a number of regional stations, we can address structural problems that are more commonly the domain of regional teleseismic tomography and surface wave tomography techniques. Our approach provides estimates on the absolute velocities in a depth range from the surface to about 200 km. By comparison, the teleseismic tomography has poor resolution at depths less than about 100 km, and in any event provides only percent variations relative to a reference velocity. Our method can image the boundary between the high-velocity mantle lid and the underlying low velocity layer. This problem is usually investigated with the aid of long period surface waves with a lateral resolution of about 1000 km. The resolution of our technique is about an order of magnitude higher.

Velocities in the upper mantle are generally high in the eastern margin of the study region (Fig. 14), in agreement with the tomographic data for the eastern Tien Shan in China [38]. The velocities are also high southwest of the study region, and may correspond to the upper mantle of the Tarim basin. High upper mantle velocities are also known to exist in the

neighboring region on the western side of the Talas–Fergana fault [22]. Our analysis confirms the conclusion of [16] that the crust in the central Tien Shan is underlain at most locations by a high-velocity lid (mantle lithosphere) several tens kilometers thick. In agreement with previous studies [22], we do not find evidence of a mantle root that might be formed by converging lithospheric plates. The upper-mantle model shows a relatively thin lid (subcrustal lithosphere) and a reduced velocity beneath the lid in the north-west of the region, where these features were already recognized in the S receiver functions of the KNET seismograph stations [16].

A thinned mantle lithosphere in the region from 41°N to 43°N between the Talas–Fergana fault and the eastern end of the lake Issyk Kul (Fig. 14) corresponds to the area of emplacement of a volumetrically small series of basaltic extrusives and intrusives of late Cretaceous–early Paleozoic age [2–4]. There is no evidence of rifting in the Tien Shan at that time, and compositions of the magmas suggest a source similar to those of ocean islands basalts [5,6]. These considerations are indicative of the presence of a small mantle plume [39]. The agitated asthenosphere and thinned lithosphere are found in the region, where they most likely were located at about 50 Ma. The coincidence suggests that the upper mantle in the northern Tien Shan might avoid a major restructuring during the subsequent orogeny. The mantle lithosphere either survived in spite of a possible partial detachment/delamination, or it was restored by subsequent plate convergence.

The southeast trending corridor of a thinned mantle lithosphere between the lake Issyk Kul and the Tarim basin (Fig. 14) is another noteworthy result of our analysis. Contrary to the area in the north, this region is devoid of indications of a recent magmatic agitation. However, the corridor nearly coincides in the Tarim basin with the Bachu uplift [40]. The uplift is expressed as a region of a reduced thickness of the Cenozoic sediments (less than 1000 m relative to several kilometers outside). The coincidence suggests that the uplift might be caused by a recent thermal agitation of the upper mantle, perhaps related to the plume in the north. A transfer of the basaltic magma to the surface might be prevented by the onset of a compressive regime in the lithosphere.

Crustal thickness (Fig. 13) is a robust result of our analysis for most stations. In most cases, it is close to that previously found from the P [15] and S [16] receiver functions. The values around 45 km are characteristic of the Kazakh shield and the Tien Shan foreland in the North and the Tarim basin in the South. Crustal thickness beneath the orogen varies in a range from about 45 km (East of the Talas–Fergana fault) to about 70 km. The smallest values that are found in a neighborhood of the Talas–Fergana fault are most likely inherited from the pre-orogenic era [14,16,26]. Interesting, on the other side of the fault at the same latitudes crustal thickness reaches 60–65 km [20], which is indicative of a different style of tectonics. The average crustal thickness beneath the orogen (around 55 km) is definitely larger than beneath the neighboring platforms, but within the orogen, it is poorly correlated with the surface topography: the values around 45 km correspond to the free surface altitudes reaching 3 km, whereas in the other terranes with comparable altitudes the thickness may reach 60 km.

The values in excess of 60 km are found beneath the ridges in the south and northwest. In the north, the largest values are documented by data from several seismograph stations: AAK, AML, EKS2, KBK, UCH, which are among the best in the region. In the corresponding velocity column (Figs. 15 and 16) the elevated crustal thickness is clearly associated with the thickened ‘basaltic’ (Vs around 4.0 km/s) layer in the lower crust and the presence of a low-velocity body in the upper mantle at a shallow depth. The anomalous thickness of ‘basalt’ is not an artifact of interpolation, as it is present in the individual models. This striking coincidence suggests that the large crustal thickness is caused, at least partly, by recent magmatic underplating. A similar coincidence is seen in the region of large crustal thickness in a vicinity of station KAR (Fig. 16), although this result is determined by the data of one station and is less reliable. These observations are consistent with the earlier suggestions of a broad gradient between the crust and mantle in the central Tien Shan [20].

The thick crust in the south is defined mainly by the data of stations AHQI, HARA, HLQI and KASH. The upper crust in this region is characterized by thin-skin tectonics of the sedimentary cover of Tarim [40]. The lower crust is dominated by a layer with “basaltic”

velocities up to 30–40 km thick (Figs. 15 and 17). Most likely, this feature is characteristic of the crustal structure of Tarim and not related directly to the present day process. Unfortunately, the data for these stations are of lower quality than those in the north.

The correlation between the maximum values of crustal thickness and of a thickened 'basalt' layer in the north, together with a general de-correlation between crustal thickness and surface relief suggest that, in addition to crustal shortening, magmatic underplating and near-vertical block movements might play a significant role in the recent tectonic evolution, especially in the north of the region. We note that similar processes are known elsewhere, for example, in the foreland of the central Andes [41].

Acknowledgements

This study was supported by GFZ Potsdam, ISTC grant KR837 and RFBR grants No. 03-05-64654 and 01-05-64381. I. Aleshin, G. Kosarev and S. Oreshin visited GFZ Potsdam, and they thank German colleagues for their hospitality. The authors appreciate a discussion of tectonics of the Tien Shan with M. R. Strecker and E. R. Sobel. The instruments used in the collection of GHENGIS data were provided by the IRIS PASSCAL program. The recordings of stations KNET, AAK, TLG and WUS were obtained from IRIS DMC. The authors appreciate comments from S. Chevrot and from an anonymous reviewer.

References

[1] V.S. Burtman, Structural geology of the Variscan Tien Shan, USSR, Am. J. Sci. 275 (1975) 157–186.
[2] G.I. Dobretsov, I.A. Zagruzina, Young basaltoid igneous activity in the eastern Tien Shan, Trans (Dokl) USSR Acad. Sci., Earth Sci. Sect. 235 (1977) 67–70.
[3] V.I. Knauf, A.V. Mikolaychuk, Y.V. Khristov, The structural position of Mesozoic–Cenozoic volcanism in central Tien Shan, in: K.Y. Kalmurzayev (Ed.), Seismotektonika i sesmichnost' Tyan-Shanya, Ilim, Frunze, 1980, pp. 3–18, in Russian.
[4] A.B. Bakirov, Geological formation map of Kyrgyzstan, Scale 1:500,000. 1 map on 10 sheets, Glavnoe upravlenie geodezii i kartografii (1988).
[5] A.F. Grachev, Early Cenozoic magmatism and geodynamics of north Tien-Shan. Izvestiya Russian academy of sciences, Phys. Solid Earth 35 (10) (1999) 815–839.
[6] E.R. Sobel, N. Arnaud, Cretaceous–Paleogene basaltic rocks of the Tuyon basin, NW China and the Kyrgyz Tien Shan: the trace of a small plume, Lithos 50 (2000) 191–215.
[7] E. Sobel, T.A. Dumitru, Thrusting and exhumation around the margins of the western Tarim basin during the India–Asia collision, J. Geophys. Res. 102 (1977) 5043–5063.
[8] K.Y. Abdrakhmatov, S.A. Aladzhanov, B.H. Hager, M.W. Hamburger, T.A. Herring, et al., Relatively recent construction of the Tien Shan inferred from GPS measurements of present day crustal deformation rates, Nature 384 (1996) 450–453.
[9] Ch. Reigber, G.W. Michel, R. Galas, D. Angermann, J. Klotz, et al., New space geodetic constraints on the distribution of deformations in Central Asia, Earth Planet. Sci. Lett. 191 (2001) 157–165.
[10] P. Tapponier, P. Molnar, Active faulting and Cenozoic tectonics of Tien Shan, Mongolia and Baikal regions, J. Geophys. Res. 84 (1979) 3425–3459.
[11] J.-P. Avouac, P. Tapponier, M. Bai, H. You, G. Wang, Active thrusting and folding along the northern Tien Shan and late Cenozoic rotation of Tarim relative to Dzungaria and Kazakhstan, J. Geophys. Res. 98 (1993) 6755–6804.
[12] K. Abdrakhmatov, R.J. Weldon, S.C. Thompson, D.W. Burbank, C.M. Rubin, M. Miller, P. Molnar, Quatitative bearing of modern movements on the deep geoelectric structure of the Earth's crust in the central Tien Shan and distribution of seismicity, Russ. Geol. Geophys. 42 (2002) 1585–1609.
[13] S.C. Thompson, R.J. Weldon, C.M. Rubin, K. Abdrakhmatov, P. Molnar, G.W. Berger, Late Quaternary slip rates across the central Tien Shan, Kyrgyz Republic, Central Asia, J. Geophys. Res. 107 (2002) 7–10 (7–32).
[14] V.N. Krestnikov, I.L. Nersesov, Tectonic structure of the Pamirs and Tien Shan and its relation to topography of the Moho boundary, Sov. Geol. 11 (1962) 36–69.
[15] S. Roecker, Constraints on the crust and upper mantle of the Kyrgyz Tien Shan from the preliminary analysis of GHENGIS broad-band data, Russ. Geol. Geophys. 42 (2001) 1554–1565.
[16] S. Oreshin, L. Vinnik, D. Peregoudov, S. Roecker, Lithosphere and asthenosphere of the Tien Shan imaged by S receiver functions, Geophys. Res. Lett. 29 (8) (2002) (doi:1029/2001GL014441).
[17] S.W. Roecker, T.M. Sabitova, L.P. Vinnik, Yu.A. Burmakov, M.I. Golvanov, R. Mamatkanova, L. Munirova, Three-dimensional elastic wave velocity structure of the western and central Tien Shan, J. Geophys. Res. 98 (1993) 15779–15795.
[18] S. Ghose, M. Hamburger, J. Virieux, Three-dimensional velocity structure and earthquake locations beneath the northern Tien Shan of Kyrgyzstan, central Asia, J. Geophys. Res. 103 (1998) 2725–2748.
[19] L.P. Vinnik, S. Roecker, G.L. Kosarev, S.I. Oreshin, I.J. Koulakov, Crustal structure and dynamics of the Tien Shan, Geophys. Res. Lett. 29 (22) (2002) 2047 (doi:10.1029/2002GL015531).
[20] G.L. Kosarev, N.V. Petersen, L.P. Vinnik, S.W. Roecker, Receiver functions for the Tien Shan analog broad-band network: contrasts in the evolution of structures across the Talas–Fergana fault, J. Geophys. Res. 98 (1993) 4437–4448.

[21] Y.A. Trapeznikov, E.B. Andreyva, V.Yu. Butalev, M.N. Berdichevsky, L.L. Vanyan, et al, Magnetotelluric soundings in the Kyrgyz Tien Shan mountains, Fiz. Zemli 1 (1997) 3–20 (in Russian).

[22] L.P. Vinnik, A.M. Saipbekova, Structure of the lithosphere and the asthenosphere of the Tien Shan, Ann. Geophys. 2 (1984) 621–626.

[23] L.I. Makeyeva, L.P. Vinnik, S.W. Roecker, Shear-wave splitting and small-scale convection in the continental upper mantle, Nature 358 (1992) 144–147.

[24] C.J. Wolfe, F.L. Vernon, Shear-wave splitting at central Tien Shan: evidence for rapid variation of anisotropic patterns, Geophys. Res. Lett. 25 (1998) 1217–1220.

[25] L. Vinnik, D. Peregoudov, L. Makeyeva, S. Oreshin, S. Roecker, Towards 3-D fabric in the continental lithosphere and asthenosphere: the Tien Shan, Geophys. Res. Lett. 29 (16) (2002) (doi:10.1029/2001GL014588).

[26] Y.H. Chen, S.W. Roecker, G.L. Kosarev, Elevation of the 410-km discontinuity beneath the central Tien–Shan; evidence for a detached lithospheric root, Geophys. Res. Lett. 24 (12) (1997) 1531–1534.

[27] L. Vinnik, Detection of waves converted from P to SV in the mantle, Phys. Earth Planet. Inter. 15 (1977) 39–45.

[28] C.A. Langston, Structure under Mount Rainier, Washington, inferred from teleseismic body waves, J. Geophys. Res. 84 (1979) 4749–4762.

[29] L. Vinnik, V. Farra, Upper mantle stratification by P and S receiver functions, Geophys. J. Int. 141 (3) (2000) 699–712.

[30] L. Vinnik, H. Chenet, J. Gagnepain-Beyneix, P. Lognonne, First seismic receiver functions on the moon, Geophys. Res. Lett. 28 (15) (2001) 3031–3034.

[31] L. Vinnik, V. Farra, Subcratonic low-velocity layer and flood basalts, Geophys. Res. Lett. 29 (4) DOI:10.1029/2001GL014064.

[32] N.A. Haskell, Crustal reflection of plane P and SV waves, J. Geophys. Res. 67 (1962) 4751–4767.

[33] L. Ingber, Very fast simulated annealing, Math. Comput. Model. 12 (1989) 967–993.

[34] L.-S. Zhao, M.K. Sen, P. Stoffa, C. Frolich, Application of very fast simulated annealing to the determination of the crustal structure beneath Tibet, Geophys. J. Int. 125 (1996) 355–370.

[35] L. Zhu, H. Kanamori, Moho depth variations in southern California from teleseismic receiver functions, J. Geophys. Res. 105 (2000) 2969–2980.

[36] B.L.N. Kennet, E.R. Engdahl, Traveltimes for global earthquake location and phase identification, Geophys. J. Int. 105 (1991) 429–465.

[37] E.H. Isaacs, R.M. Srivastava, Applied Geostatistics, Oxford University Press, New York, 1989.

[38] G. Poupinet, J.-P. Avouac, M. Jiang, S. Wei, E. Kissling, et al, Intracontinental subduction and Palaeozoic inheritance of the lithosphere suggested by a teleseismic experiment across the Chinese Tien Shan, Terra Nova 14 (2002) 18–24.

[39] N.L. Dobretsov, M.M. Buslov, D. Delvaux, N.A. Berzin, V.D. Ermikov, Meso-and Cenozoic tectonics of the central Asian mountain belt; effects of lithospheric plate interaction and mantle plumes, Int. Geol. Rev. 38 (1996) 430–466.

[40] D. Li, D. Liang, C. Jia, G. Wang, Q. Wu, D. He, Hydrocarbon accumulation in the Tarim basin, China, AAPG bull. 80 (10) (1996) 1587–1603.

[41] M.R. Strecker, P. Cerveny, A.l. Bloom, D. Malizia, Late Cenozoic tectonism and landscape development in the foreland of the Andes: northern Sierras Pampeanas (26°–28°S), Argentina, Tectonics 8 (1989) 517–534.